Spintronic Properties in Complex Perovskites: A Concordance Between Experiments and Ab-Initio Calculations

J. Roa-Rojas, C. E. Deluque Toro, A. V. Gil Rebaza, X. A. Velásquez Moya, and D. A. Landínez Téllez

Abstract Complex perovskite-type compounds constitute one of the most exciting families of materials due to the wide range of applications such as anode materials for solid oxide fuel cells, highly active catalysts in electrochemical energy conversion reactions, substrates for high-efficiency solar cells, piezoelectric or dielectric sensors, magnetoelectric and magnetoresistive devices, magnetic and spintronic semiconductors with uses in dynamic random access memories (DRAM) or non-ferroelectric random access memories (NVFRAM), hard disk read–write heads for high capacity storage of information in magnetic media and devices for electron current polarization, magnetic sensors, among others. In the present chapter we will focus on the study of the structural, magnetic, ferroelectric, semiconducting and thermophysical properties of complex perovskites with general formula $A_2BB'O_6$ where A are alkaline earth elements, rare earths or metals of large ionic radius and B and B' are some transition metal elements. For this purpose, we present an exhaustive theoretical–experimental study of these compounds, reporting responses in measurements with different experimental techniques, correlated to ab-initio calculations in the framework of the Density Functional Theory and thermodynamic properties by means of Debye's quasi-harmonic model. The obtained results reveal the applicability of various complex perovskites in the spintronics industry.

J. Roa-Rojas · X. A. V. Moya · D. A. L. Téllez
Grupo de Física de Nuevos Materiales, Departamento de Física, Universidad Nacional de Colombia, 111321 Bogotá, D.C, Colombia

C. E. D. Toro
Grupo de Nuevos Materiales, Facultad de Ingeniería, Universidad del Magdalena, Santa Marta, Colombia

A. V. G. Rebaza (✉)
Departamento de Física, Facultad de Ciencias Exactas de la Universidad Nacional de La Plata UNLP, 1900 La Plata, Argentina
e-mail: arvifis@gmail.com

Instituto de Física La Plata - IFLP, CCT La Plata CONICET, 1900 La Plata, Argentina

D. A. L. Téllez
Grupo de Estudios de Materiales GEMA, Departamento de Física, Universidad Nacional de Colombia, 111321 Bogotá, D.C, Colombia

C. A. Taft and S. R. de Lazaro (eds.), *Research Topics in Bioactivity, Environment and Energy*, Engineering Materials, https://doi.org/10.1007/978-3-031-07622-0_6

1 Introduction

The applications of electric charge transport in materials have been known since before the discovery of the electron at the end of the nineteenth century. However, its special applicability in what is known as "electronics" took place in the twentieth century. Electronics, defined as that part of physics that studies the controlled transport of electric charges by means of the laws of electromagnetism, was first associated with vacuum physics, giving rise to electronic devices based on tubes with diode and triode functionality, among others, with which oscillators, amplifiers and modulators were produced.

Around the 1930s, the semiconducting properties of Si and Ge became known, giving rise to p-n junctions and the creation of the first transistor in the 1940s. From that moment on, advances in solid-state physics modified electronics as it was previously known, drastically changing the applications of semiconductor materials, creating new, more efficient and functional devices, and promoting successive miniaturization processes that turned it into microelectronics in the 1950s. Thus, individual components were replaced by the integrated circuit or chip: a Si crystal of small dimensions, containing tiny capacitors, diodes, resistors and transistors appropriately interconnected. These processes were the direct promoters of the transformation between analog and digital processing, with an unusual growth in the 60's and 70's that led to the evolution of microprocessors used in personal computers and following the so-called G.E. Moore's law [1]. At the beginning of this century, the design of processors with nanometer technology (90 nm) gave rise to the so-called nanoelectronics, which gave rise to a race among large companies producing devices for information processing and storage, including USB memories, portable hard disks and innovations in cell phones, among others [2].

Up to this point, the functionalities in electronic devices were obtained by controlling the electron charge transport, aided by semiconductor materials in processing and logic operation [3]. On the other hand, the storage of information, as well as the processes of reading, writing and erasing it, was introduced through the use of magnetic materials [4]. Recently, a new word related to the intrinsic properties of the electron has made the old electronics reach unsuspected levels of applicability and multifunctionality: spintronics. Spin transport electronics (spintronics) is that in which the manipulation of the electron spin and the resulting magnetic moment allows the modification of the functionalities of materials, facilitating the design of more versatile and faster devices than their predecessors and giving rise to a technology in which, in addition to the control of the fundamental charge, the intrinsic spin and the magnetic moment of the electron are controlled [5]. The generation of spin currents can be performed by injection of magnetic spins from a ferromagnetic material, the application of electric and magnetic fields, the introduction of electromagnetic waves, the inclusion of elements that promote Zeeman splitting, the application of thermal gradients and mechanical rotations or geometric modifications [6]. These spin current generation methods applied to the design of spintronic devices are intrinsically related to exotic properties such as giant [7] and colossal

[8] magnetoresistance, half-metallicity [9], exchange-bias [10] multiferroicity [11] and coexistence of ferromagnetism and semiconductivity [12], among others. The design of new magnetic semiconductor materials that allow the control of logic operations as well as the reading and recording of information in a single material could substantially simplify the development of spintronic devices. Efforts to reconcile the two properties, semiconductivity and magnetism, in a single functional material started with the epitaxial growth of tetrahedrically coordinated semiconductor films containing magnetic transition metals [13], up to the so-called dilute magnetic semiconductors, in which spin-dependent magneto-electro-optical properties can be observed [14, 15]. The main obstacle of applicability in spintronic devices at room temperature of the former lies in the difficulty to increase the densities of the included transition metals and hollow carriers [14], while in the latter the major difficulty has to do with the spin-dependent coupling between the semiconductor bands and localized states, which occurs because many of the magnetic particles are not part of the structure of the semiconductor material and remain interstitial or form secondary crystallographic phases [16].

In the present chapter, two ceramic material systems are presented that show semiconducting and ferromagnetic behaviors simultaneously in a single crystalline structure, which may represent an excellent perspective in the generation of new multifunctional materials for applications in spintronic devices. These materials belong to a particular family of oxides known as perovskites [17], which, due to their particular crystallographic characteristics, allow the inclusion of alkaline earth cations, rare earths and transition metals, so that the physical properties can be tuned by modifications in the stoichiometric composition and structural variations of the material [18]. An advantage of perovskites is that their degree of structural complexity depends on the type of substitutions that can be made from their basic formula, which, in turn, allows modifying and even predicting the occurrence of physical properties in new materials [19].

One family of versatile materials that represents a large percentage of the systems currently being investigated in solid physics and chemistry is the so-called perovskites. In general, perovskites are represented by the ideal formula ABX_3, where A is an alkali earth element, a rare earth, or a metal or semimetal of large ionic radius, B represents a transition metal or lanthanide element, and X, usually, is oxygen or a halogen [20]. Modifications of the atomic radii of A and B introduce structural distortions and new crystalline phases, while inclusions of rare earth elements give the possibility to produce materials with exotic electrical and magnetic properties [21]. Partial substitutions of the A and B cations give rise to complex materials such as double perovskites with generic formula $A_2BB'O_6$ [22] and even more complex perovskites $AA'B_2O_6$ [23] and the well-known triple perovskite $A_2A'B_2B'O_9$ [24]. Their chemical configuration offers multiple possibilities to combine different elements, as well as the possibility to synthesize new materials with a wide variety of physical properties. Depending on the magnetic and electrical characteristics of A, A', B and B' it is relatively easy to create new perovskite systems with promising prospects in the new field of spintronic technology [25]. In the $A_2BB'O_6$ double perovskites it is possible to obtain materials evidencing

B-B' cation ordering along the crystallographic axes, forming a salt-rock type structure [26], which is not the case for other types of complex perovskite [27]. These structural characteristics limit the crystalline symmetries for the different families of complex perovskites, suggesting the occurrence of structural distortions that also correspond to octahedral inclinations and rotations that influence the physical properties as a result of the intrinsic characteristics of the constituents of the material [28].

Double perovskite-type materials will be presented in this chapter, which are generated from the general formula $A_2BB'O_6$. As can be inferred from the title of the chapter, experimental results suggesting macroscopic behaviors applicable in spintronics will be presented. Results of structural properties and electrical, magnetic and optical responses for materials belonging to these families of perovskite-type materials will be duly correlated with predictions from calculation of density of electronic states. These will be performed by means of Density Functional Theory (DFT), which has become a potentially powerful tool for predicting physical properties in perovskite-type materials [29]. Additionally, considering that the macroscopic thermodynamic properties are strongly correlated with the microscopic dynamics of the atoms of the material, and assuming that the collective vibrations of the crystal lattices in these solid materials take place via phonons, it is possible to study the fundamental excitations that are associated with these thermodynamic properties. The most representative function of phonons takes place in insulators and semiconductors, where they make direct contributions to properties such as specific heat and thermal expansion, indicating that they are temperature-dependent properties. In relation to phonons, vibrations in perovskite-type crystals will be considered to have a harmonic character, which will be valid for temperature values below the Debye temperature of the solid. In this way, theoretical methods can constitute a complementary tool for the study of atomic dynamics at relatively high temperatures, through approximations such as the quasi-harmonic Debye model [30]. Thus, the results of the density of electronic states and the behavior of specific heat, Debye temperature, entropy, thermal expansion and the Grüneisen parameter as functions of pressure and temperature will be presented.

The single perovskite-type material $LaFeO_3$, known as lanthanum orthoferrite, has been extensively investigated for more than 60 years because of its G-type antiferromagnetic character [31], as well as for simultaneously exhibiting weak ferromagnetic [32] and ferroelectric [33] responses, so it can be classified as a multiferroic material [34]. Experimentally, the lanthanum orthoferrite $LaFeO_3$ adopts an orthorhombic crystal structure, belonging to the space group Pnmb (# 62), with tolerance factor $t = 0.951$ and octahedral distortions given by $a^+b^-b^-$ [35]. On the other hand, the so-called lanthanum cobaltite $LaCoO_3$ has been studied since 1953, showing a total effective magnetic moment greater than the value expected from Hund's rules and Co^{3+} electronic spin splittings [36]. Initially, the suggested explanations for this effect were based on contributions due to the appearance of Co^{3+} ions in the structure in octahedrally coordinated sites under strong crystal field intensity [37] and spin–orbit type effects, considering a cubic perovskite type structure with trigonal distortions [38]. The exotic electrical and magnetic properties, as well as the different

possible interactions, including the coexistence of low and high spin configurations of the Co cation have been analyzed for many years, including theoretical studies of electronic structure with variations in possible spin configurations and proposals for the occurrence of a transition between a low spin configuration and an intermediate spin state [39]. Despite the apparent similarity in the chemical formula of lanthanide cobaltite and lanthanide orthoferrite, $LaCoO_3$ crystallizes in a rhombohedral structure, belonging to space group R-3c (# 167), with a tolerance factor t = 1.012 and out-of-phase distortions on the three octahedral sub-axes according to Glazer's $a^-a^-a^-$ notation, showing a mostly antiferromagnetic ordering, with incipient ferromagnetic coupling [40] and dielectric response [41]. The interesting properties exhibited by these two materials, as well as their substantial structural differences, in addition to the magnetic nature due to the crystalline field and the types of bonding of the Co^{3+} and Fe^{3+} cations with oxygen in the Co-O_6 and Fe-O_6 octahedra, have direct inference on the exotic physical properties they exhibit. These are the reasons why it is of particular interest to study a complex perovskite-type material from the union of these two simple perovskites to produce the double perovskite La_2CoFeO_6 [42]. On the other hand, from the theoretical point of view, the correct determination of the electronic structure of materials containing 3d elements such as Co and Fe in the structure is not easy because of the complex splitting of low spin and high spin electrons due to the crystal field and their interactions with the oxygens in the tetrahedral coordination. Although some calculations have been reported [43], the Hubbard potential applied may not have been exactly the best fit to the experiment, so it is important to revisit the applied concepts, as well as the correction to the exchange potential and correlation considered in the calculations. When La is substituted by rare earths in orthoferrite, its structure remains [44] but its magnetic response depends on the specific cation, showing antiferromagnetism for R = Er, Dy [45], ferrimagnetism for R = Sm [46] and ferromagnetism for R = Tb [47]. On the other hand, the rare earth cobaltite $RCoO_3$ crystallizes in an orthorhombic structure (space group Pbnm, #62), evidencing different magnetic responses depending on the cation R [48], with non-collinear antiferromagntism-type character for R = Tb [49]. Due to the ferromagnetic character of the orthoferrite $TbFeO_3$ and antiferromagnetic character of the cobaltite $TbCoO_3$, the study of the double perovskite Tb_2FeCoO_6 is particularly interesting [50].

Therefore, the investigation of these materials, whose magnetic and electrical transport properties may have interesting implications for the prospects of application in spintronics technology, is of special interest.

2 Experimental Techniques

$(La,Tb)_2FeCoO_6$ samples were produced via the solid reaction method starting from powdered oxides of $(La,Tb)_2O_3$, Fe_2O_3 and Co_2O_3 (Sigma-Aldrich, > 99.99% purity). The precursor oxides were dried at a temperature T = 120 °C, then weighed in stoichiometric proportions, using an analytical balance of 0.1 mg accuracy. The

mixture obtained was crushed in an agate mortar for 3 h. The resulting homogeneous powders were heated at 600 °C for 24 h in a Lindberg-Blue tube furnace, after which it was remixed for 30 min and pressed under the application of 4.5 kN in a 9 mm diameter die to form cylindrical tablet-shaped samples. The samples were then subjected to thermal sintering processes at 800 °C, 1000 °C and 1200 °C for 24 h each to ensure the grain growth process and densification of the samples. The structural analysis of the samples was performed by means of a PANalytical X'pert-Pro X-ray diffractometer ($\lambda_{CuK\alpha} = 1.540598$ Å), in Bragg–Brentano configuration, with step of 0.001° in 2θ and time of 10 s. The structural analysis was performed by Rietveld type refinement to determine crystallographic properties of the material. For the surface morphological study, images were taken by scanning electron microscopy (SEM) in a Vega 3 TESCAN equipment. A semi-quantitative electron energy dispersive X-ray energy dispersive spectroscopy (EDS) analysis was performed to determine the composition of the samples. Complex impedance measurement as a function of temperature was carried out using an Agilent-4194A phase gain and impedance analyser, a Janis Research cryogenic system (VPF-475 model) and a Lake Shore 332 temperature controller. These measurements were performed at a temperature variation rate of 1.7 K/min and in a frequency range between 102 and 107 Hz. The I-V curve at room temperature was elaborated from the data measured in a Keithley-6517A DC electrometer and a sample holder with gold-plated silver contacts designed by the authors, which was adapted to the cryogenic system and the temperature controller. The band gap and energy excitation regimes at room temperature were examined by using a VARIAN Cary 5000 UV–Vis–NIR diffuse reflectance spectrophotometer (DRS), which has an integration sphere with a PMT/Pbs detector. The magnetic response was evaluated by means of magnetization measurements as a function of temperature, following the Zero Field Cooling (ZFC) and Field Cooled (FC) procedures under the application of varying magnetic field strengths. Likewise, magnetic hysteresis measurements were performed, varying the applied field intensity in isothermal curves at different temperatures. The equipment used to measure the magnetic response was a VSM-PPMS Quantum Design. Various temperature and applied field regimes were considered for the different measured samples.

3 Calculation Methods

As mentioned above, the calculations were performed by means of DFT, since it has been proven that in perovskite-type materials its results agree with those obtained experimentally [51–54]. For the study of the structural, cohesive, electronic and thermodynamic properties of complex perovskites, the VASP code was used, which is based on DFT and the Augmented Wave Projector (PAW) [55–60]. Since the Generalized Gradient Approximation (GGA) does not fully describe the system containing 3d-Fe, 3d-Co and 5d-La orbitals, the exchange and correlation energy was evaluated using the GGA with the inclusion of corrections to the Hubbard U potential (GGA + U) [50–54, 61]. Due to the ferromagnetic characteristic of the material, the value of U

was obtained following the method described for this type of magnetic ordering [62], finding optimal potentials $U_{Fe} = 5.3$ eV for Fe and $U_{Co} = 3.32$ eV for Co. The ion–electron interactions were described through the PAW [57–59] and all calculations were performed considering spin-polarized configurations. The kinetic energy cutoff for the plane wave expansion of the electronic wave function was 520 eV. Gratings of k-points defined according to the Monkhorst–Pack method [63] were used, where the convergence of the gratings was verified until an energetic accuracy higher than 1 meV/atom was obtained. The Methfessel-Paxton technique [64] with a mixing factor of 0.1 eV was adopted for filling the electronic levels. For these configurations, grids of $9 \times 9 \times 7$ k-points were considered. These grids represent 284 k-points in the irreducible Brillouin zone. The conjugate gradient method was used to find stable ionic positions, with an energy value of 0.1 meV used as the convergence criterion for the total self-consistent energy calculations. The lattice parameters and internal coordinates of the unit cell were fully optimized by maintaining the spatial symmetry group of the crystal structure, until the forces were less than 30 meV/Å and the energy due to ionic relaxation was less than 1.0 meV/atom. These calculations were performed considering a monoclinic crystalline structure with space group $P2_1/n$ (#14), in agreement with experimental results for $(La,Tb)_2FeCoO_6$ [42, 59]. To determine the Density of States (DOS) parameters, the total energy (E) and external pressure (P) were calculated for different volumes (V) varying around the equilibrium volume (V_0) up to $\pm$ 5%, allowing relaxation of the internal coordinates. The bulk modulus (B_0) and its pressure derivative (B') were obtained by fitting the pressure curves as a function of volume from the Murnaghan equation of state [65].

For the materials for which thermodynamic property calculations were performed, these were carried out following the Debye quasi-harmonic model [66, 67]. In this model, macroscopically measurable thermophysical properties are directly associated with the microscopic dynamics of the atoms within the material when subjected to external changes in pressure and temperature. Considering that the collective vibrations of the crystalline cells of solids occur in the form of phonons, the fundamental excitations associated with these thermodynamic properties can be comfortably calculated. In materials evidencing relatively high electrical resistivities, phonons play a particularly important role, giving relevant contributions to some properties such as specific heat and thermal expansion as a function of temperature. In this way, the crystal lattice vibrations can be expected to exhibit a harmonic character for temperature values below the Debye temperature of the material. In this work, the Debye quasi-harmonic model is applied as part of the study of atomic dynamics in the appropriate temperature regime.

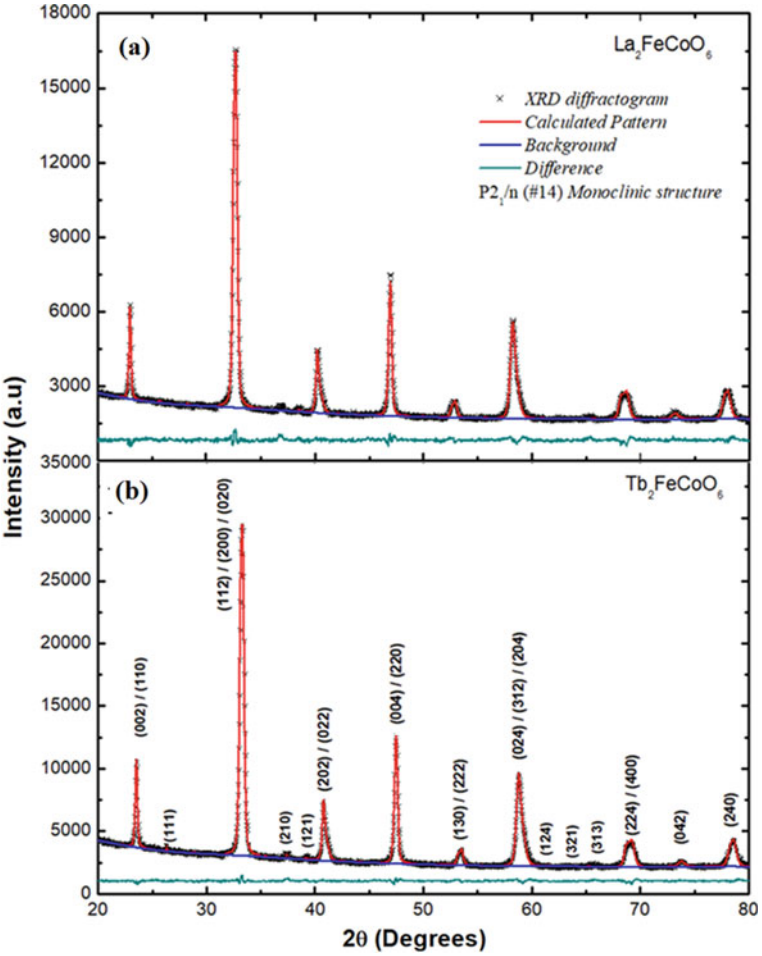

Fig. 1 Diffraction patterns obtained for materials **a** La_2FeCoO_6 and **b** Tb_2FeCoO_6

4 Semiconductor Ferromagnetic Features and Thermophysical Properties of Superstructurated $(La,Tb)_2CoFeO_6$ Double Perovskites

4.1 Structural Characteristics

The diffraction pattern shown in Fig. 1 was obtained under the same instrumental conditions specified in Sect. 2. Close observation of the diffractograms reveals practically the same reflection peaks for the materials La_2FeCoO_6 and Tb_2FeCoO_6, corresponding to perovskite-type monoclinic structure belonging to the $P2_1/n$ (#14) space group.

Although the structure is the same, for R = Tb a shift of the diffraction peaks to the right with respect to R = La is observed, which is related to the change in lattice parameters, as presented in Table 1 and Fig. 2, where the atomic distribution is exemplified from the results of the Rietveld analysis. This shift is related to a contraction of about 3% in the crystallographic cell of the material for R = Tb with respect to R = La. The structure depicted in Fig. 2 corresponds to a monoclinic perovskite, belonging to space group $P2_1/n$, which characterizes a primitive cell with rotational symmetry of two orders of 180° around a screw-shaped axis, a subsequent translation of half a cell parameter in the [010] direction and a sliding reflection plane perpendicular to the [010] direction.

The differences between the ionic radii of the constituent atoms of the material, together with the bond characteristics and electronic correlations, as well as the crystal field effects due to the presence of 3d orbitals in the octahedral coordinations, cause rotations and tilts of the octahedra that influence the magnetic and electric transport responses of the material. In Glazer's notation for octahedral distortions [68], this structure corresponds to the system denoted $a^-b^+a^-$, where the superscripts (+) indicate in-phase tilt and (−) out-of-phase tilt. Therefore, in the R_2FeCoO_6 material the octahedra rotate out of phase along the *a* and *c* crystallographic axes, while they rotate in phase along the *b* axis. This is corroborated by the appearance of indexed reflections such as (004), (204) and (404) observed in Fig. 1, which are directly related to the in-phase octahedral tilt (*ood*) along the direction of the *b* cell parameter.

Table 1 Lattice parameters, crystal distances and bond angles obtained from the Rietveld refinement

Cation	Anion	Distance (Å)	Bond angles degrees (°)	
La_2FeCoO_6 crystal parameters; monoclinic angle 90.121(5)°				
Fe	O(1)	2.0250	φ_1	162.7
Fe	O(2)	2.0187	φ_2	162.7
Fe	O(3)	2.0107	φ_3	162.8
			Cell parameters (Å)	
Co	O(1)	1.8893	*a*	5.467(2)
Co	O(2)	1.8963	*b*	5.505(8)
Co	O(3)	1.9020	*c*	7.750(3)
Tb_2FeCoO_6 crystal parameters; monoclinic angle: 89.983(5)°				
Fe	O(1)	2.0159	φ_1	149.9
Fe	O(2)	2.0151	φ_2	150.5
Fe	O(3)	2.0157	φ_3	150.3
			Cell parameters (Å)	
Co	O(1)	1.8935	*a*	5.251(2)
Co	O(2)	1.8931	*b*	5.437(5)
Co	O(3)	1.8938	*c*	7.550(3)

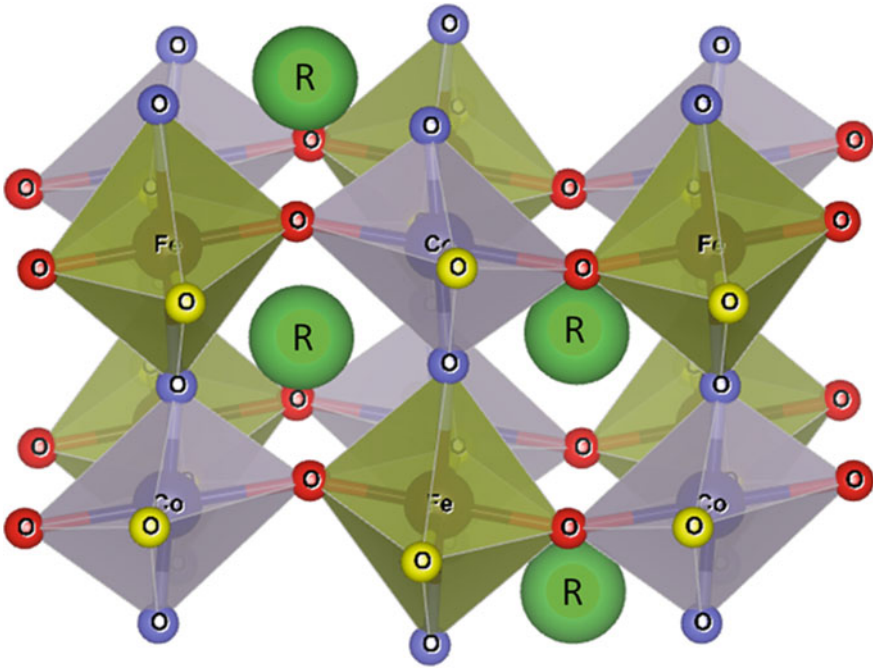

Fig. 2 Crystallographic structure of R_2FeCoO_6 (R = La,Tb) established from Rietveld refinement of XRD experimental data

Table 1 shows evident differences in the Fe-O and Co-O interatomic distances for the three sub-axes, as well as in the φ_i bond angles, both for R = La and R = Tb. These differences, which can be clearly seen in Fig. 3, have an impact on the so-called tolerance factor [69, 70]. The obtained values $\tau_{La} = 0.978$ and $\tau_{Tb} = 0.921$ are far from the ideal value ($\tau = 1$) corresponding to the cubic perovskite structure, evidencing the degree of structural distortion of the materials analyzed. Meanwhile, the presence of the incipient peaks (111) and (313) in the diffraction pattern suggest reflections due to the occurrence of cation ordering due to the formation of a superstructure with the Fe and Co cations alternating along the crystallographic axes [71, 72].

4.2 Ferromagnetic Behavior

A first part in the process of studying the magnetic response is shown in Fig. 4, where graph 4a presents the magnetic susceptibility R = La, in a temperature range between 50 and 330 K, under the application of magnetic fields of 0.5, 2.0 and 10 kOe, while graph 4b shows the magnetic susceptibility for R = Tb, in the temperature range 5 K < H < 340 K and in external fields of 2.0, 5.0, 10 and 20 kOe. In both cases

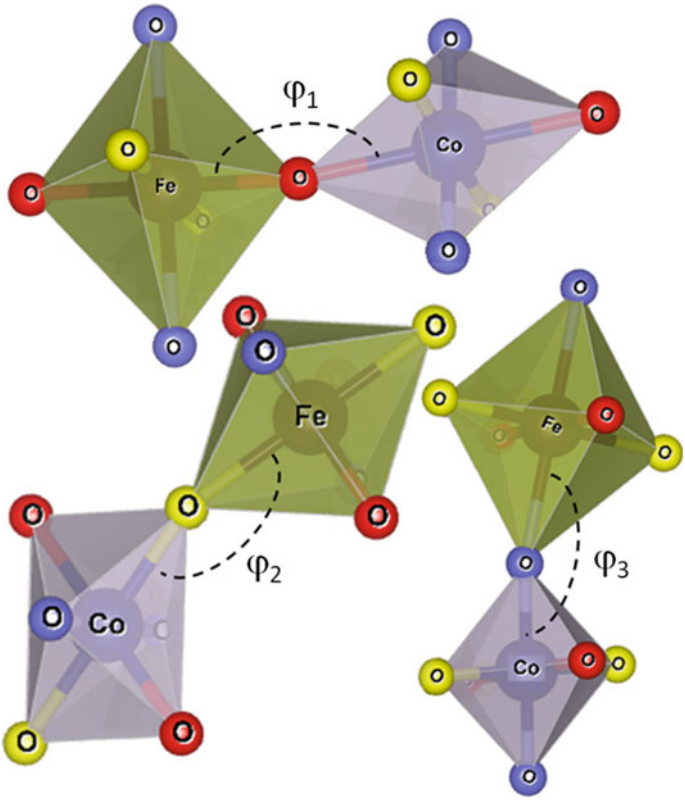

Fig. 3 Fe-O_1-Co, Fe-O_2-Co and Fe-O_3-Co bond angles between Fe-O_6 and Co-O_6 octahedra in the R_2FeCoO_6 double perovskites

the thermal procedures applied were the well-known Zero Field Cooling (ZFC) and Field Cooled (FC). For both R = La and R = Tb, the difference in the magnetic field trajectory as a function of temperature between the ZFC and FC recipes suggests the occurrence of some kind of magnetic disorder giving rise to irreversibility effects, with typical features of spin glasses [73]. In double perovskite-type materials, this behavior is attributed to the cationic disorder of the B and B' ions in the $A_2BB'O_6$ structure [54]. Meanwhile, for R = La it is not possible to establish the value of the irreversibility temperature, while for R = Tb it can not only be determined but it also evidences a shift towards the lower temperature regime with increasing applied field. This result reveals that the material with R = Tb contains a higher cationic ordering of Fe and Co ions than the compound with R = La. In this ordering, the Fe and Co cations tend to intercalate along the crystallographic axes, ensuring a higher correlation between their magnetic moments in the unit cell and along the whole structure, while the lack of correlation between the magnetic moments in the R = La is due to the low tendency of the crystalline arrangement to form a salt-rock type

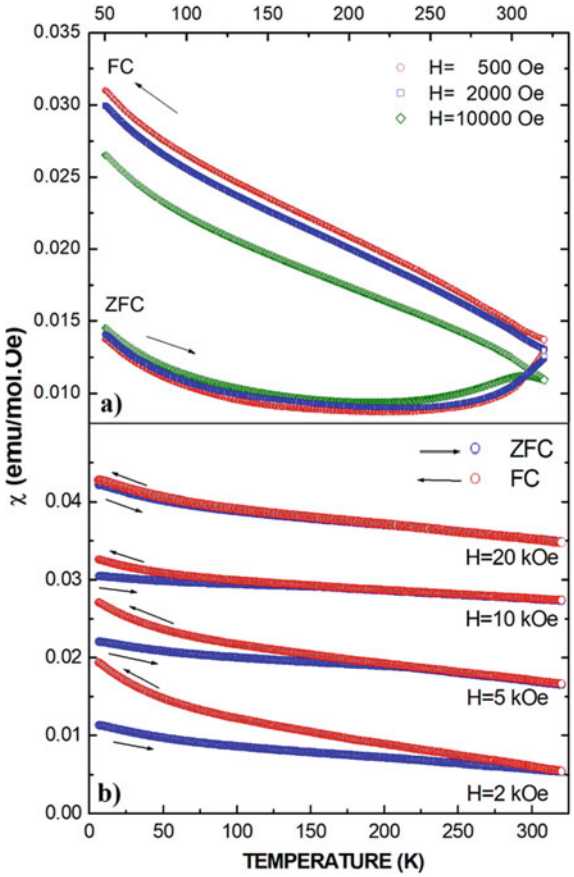

Fig. 4 Magnetic susceptibility measured at low temperatures under the application of various magnetic field intensities for La_2FeCoO_6 (**a**) and Tb_2FeCoO_6 (**b**) double perovskites

superstructure [74]. Due to the non-formation of a superstructure in which the FeO_6 and CoO_6 octahedra adopt an alternating distribution along the structure causes the breakdown of the correlation between magnetic domains, which is characteristic of ordered ferromagnetic materials, so that the ferromagnetism remains in the material but the lack of correlation between domains gives rise to the difference between the ZFC and FC responses in magnetic susceptibility. Evidence for this interpretation is in the presence of the peak (111) in the diffractogram corresponding to R = Tb in Fig. 1b that is not observed in Fig. 1a for R = La, and which is the fingerprint of cation-ordered superstructure formation in double perovskites [75].

The irreversible character could also be associated with effects due to octahedral distortions such as the tilts and rotations of FeO_6 and CoO_6, which take place in phase along the b-direction of the subcell of the octahedrons and out of phase in the a and c directions, introducing blocking of the magnetic domains at low temperatures and making it difficult to align the moments with the applied field during the ZFC procedure. The occurrence of irreversibility only takes place in the ferromagnetic

state, which allows classifying this material and can be corroborated through the finite value of magnetization observed in the susceptibility curves for the two materials under study. This magnetically ordered behavior occurs throughout the temperature region under study. The experimental confirmation of the ferromagnetic response in the two compounds was carried out by measurements of magnetization as a function of the applied magnetic field in isothermal curves at 50, 100, 200 and 300 K for R = La (Fig. 5a) and 5, 25, 50, 100, 200 and 300 K for R = Tb (Fig. 5b). The applied external field regime was -40 kOe < H < 40 kOe.

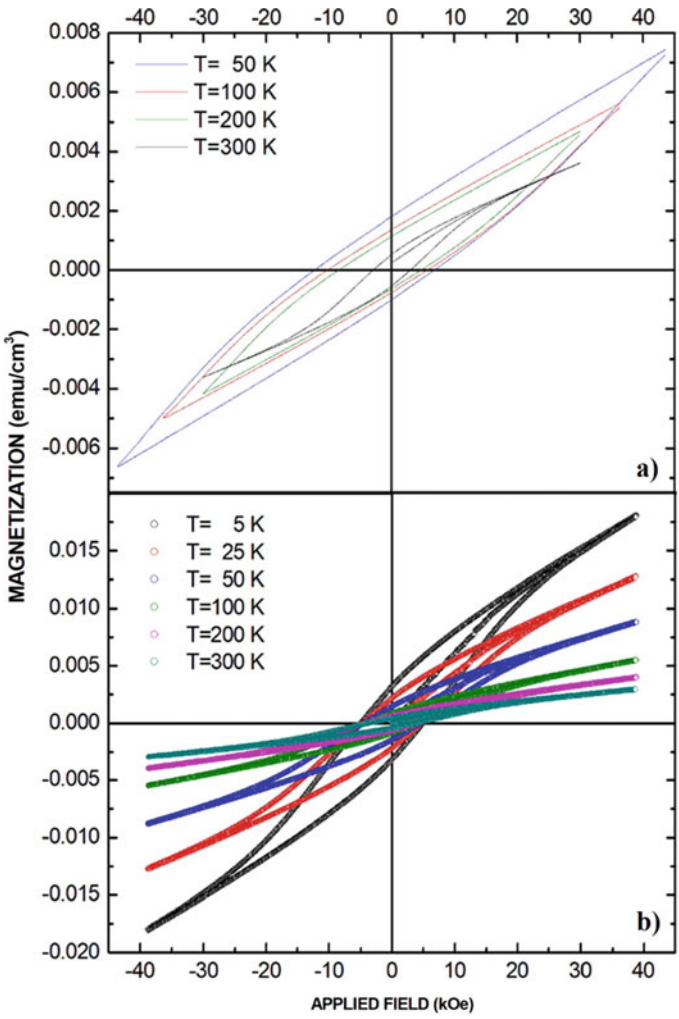

Fig. 5 Hysteretic magnetization curves as a function of applied magnetic field for rare earth ferrocobaltite with R = La (**a**) and R = TB (**b**)

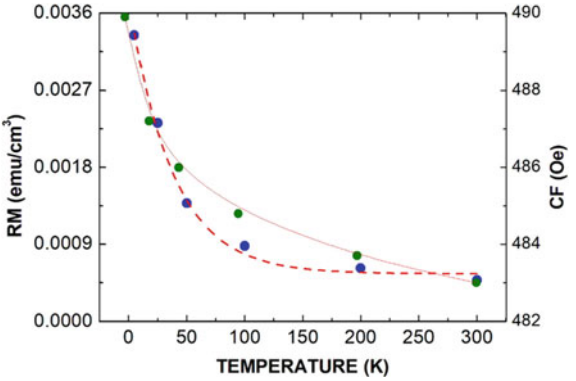

Fig. 6 Decrease in remnant magnetization (left scale) and coercive field (right scale) values with increasing temperature for double perovskite-type lanthanide ferrocobaltites

As predicted from the magnetic susceptibility curves, Fig. 5 evidences a clearly hysteretic behavior characteristic of a ferromagnetic type response for all cases studied at room temperature and below for both R = La (Fig. 5a) and R = Tb (Fig. 5b). Similarly, it is observed that with increasing temperature, there is a decrease in the number of aligned magnetic domains because the increase in entropy decreases the effective exchange energy that characterizes the ferromagnetic feature. For this reason, with increasing temperature, not only the magnetization decreases, as previously observed in the susceptibility curves, but also the magnetic energy of the system decreases as evidenced in the area enclosed by the hysteresis curve. Therefore, the characteristic magnetic parameters are proportionally affected by the change in temperature, observing a systematically decreasing behavior of the coercive field (CF) and remnant magnetization (RM) values. The behavior of the coercive field and remanent magnetization with change in temperature is shown in Fig. 6.

The response obtained for R_2FeCoO_6 decays exponentially, following an empirical law, where, $M_o{}^{La} = 1.12\ emu/g$ and $M_o{}^{Tb} = 2.73\ emu/g$ represent the spontaneous remanent magnetization for R = La and R = Tb at T = 0 K, $a_{La} = 2.15\ emu/g$ and $a_{Tb} = 15.86\ emu/g$ are phenomenological constants and $k_B T_o{}^{La} = 1.14 \times 10^{-22}\ J$ and $k_B T_o{}^{Tb} = 5.52 \times 10^{-22}\ J$ are the magnetic interaction energy corresponding to the exchange potential between the ferromagnetic moments. The obtained value is lower than the energy values calculated for the interaction between ferromagnetic spins in Fe ($12.1 \times 10^{-22}\ J$) and Co ($51.5 \times 10^{-22}\ J$) [76], showing that the ferromagnetic interaction in Tb_2FeCoO_6 requires a lower energy cost than in monatomic systems of Fe or Co. Likewise, the coercive fields vary slightly with increasing temperature but decays roughly following Kneller's law [77, 78] given by, where $H_o{}^{La} = 108.16\ Oe$ and $H_o{}^{Tb} = 492.64\ Oe$ represent the coercive fields independent of temperature, $T_B{}^{La} = 0.0011\ K$ and $T_B{}^{Tb} = 0.0035\ K$, are the blocking temperatures due to the granular feature of the samples, and $a^{La} \approx 0.35$ and $a^{Tb} \approx 0.5$ are the Bloch's exponent, which has been observed in ferromagnetic nanoparticles randomly oriented [79], multilayers [80] and bulk spinels [81], suggesting that the variation of the coercive field is sensitive to thermal activation mechanisms, with contributions due to the

occurrence of magnetic multidomain states due to the microstructural anisotropy of crystallites and grains in the material [77].

4.3 Electric Response

I-V response measurements were experimentally elaborated with the objective of analyzing the behavior of the electrical response of the materials at room temperature, under application of voltage ranges between −400 V and 400 V for R = La and between −200 V and 200 V for R = Tb. The curves obtained are shown in Fig. 7, which clearly shows that the change in applied voltage causes a nonlinear response of the current in the material. The trend followed by the curve has the characteristics observed in varistor type semiconductors [53]. As the voltage increases, the current increases following a power law of the type. Initially, increasing the voltage induces

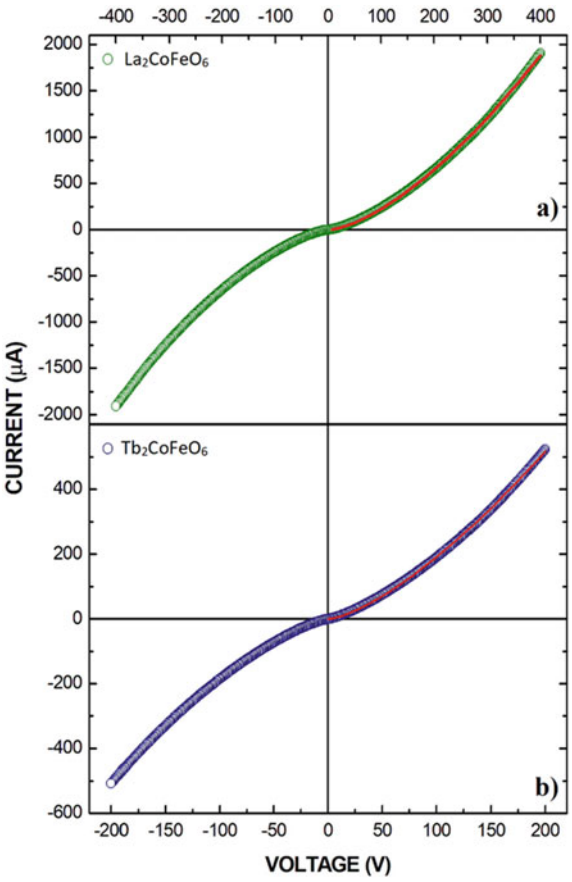

Fig. 7 I-V characteristic curves measured on La_2FeCoO_6 (**a**) and Tb_2FeCoO_6 (**b**) samples

small currents due to the occurrence of polarization effects and mixing between dielectric responses and granular boundary relaxation effects. Subsequently, electrons promoted across the gap from the semiconductor valence band conduct, tending to linearize the behavior of the I-V curve for high applied voltages. The fit with the potential spike for the two materials yields the following results: $I_o{}^{La} = 0.19\ mA$, $I_o{}^{Tb} = 0.27\ mA$ and $b» 1.53$, $b^{Tb}» 1.43$. This behavior implicitly contains an additional thermal response that contributes to deviating the electrical response from Ohm's law. Thus, the power dissipation is expected to increase rapidly as the applied voltage increases. The dissipation, then, has contributions due to the appearance of Schottky barriers formed by the grain boundaries, which give rise to the nonlinear characteristic of the I-V curve [53]. These barriers are formed by micro-junctions in which a pair of grains can be seen as two consecutive Zener diodes, such that the intergranular boundaries along the material adopt the behavior of resistors that generate currents like those expected in a varistor diode. For high voltage values, the resistance follows the expected ohmic trend, but in this regime the resistivity decreases because the intragranular contributions are more relevant than the intergranular ones. Therefore, the electrical transport due to microstructural defects can be modeled through equivalent electrical circuits that are related to the intra- and intergranular transport currents within the material [82]. According to the model, the I-V figure of merit of the varistor has the form of a power law, as mentioned above, where Io is a free constant corresponding to the nonlinear coefficient, whose value close to 3/2 is predicted by the quasi-hydrodynamic equations of semiconductors and was attributed to regions of the sample with evanescent carriers [83, 84].

4.4 Electronic Structures

It is well known that the macroscopically observable properties of perovskite-type materials can be explained through the study of their electronic behavior [85, 86]. For this reason, the density of electronic states of the compounds R_2FeCoO_6 following the procedure detailed in Sect. 3. The base magnetic state of the material was considered through ferromagnetic coupling between Fe-O-Fe, Fe-O-Co and Co-O-Co atomic bonds, in addition to possible antiferromagnetic ordering configurations between the aforementioned atoms. In order to explore different configurations of antiparallel spin distribution in the [001], [110] and [111] directions for the antiferromagnetic coupling cases, a $2 \times 2 \times 2$ supercell of the double perovskite was used. For the ferromagnetic case, all the spins due to the magnetic moments of Fe and Co atoms were considered to be oriented in the direction of application of the external magnetic field. By minimizing the energy for all the mentioned cases, the result reveals that the lowest energy distribution corresponds to a ferromagnetic type of exchange interaction. Since the GGA does not satisfactorily describe the system for the 3d-Fe, 3d-Co, 5d-La and 4f-Tb orbitals, it became necessary to calculate the exchange and correlation energy by means of the generalized gradient approximation including the Hubbard U-correction (GGA + U) [87]. From the ferromagnetic nature of the material, evidenced

both in experimental results and by the energy minimization process, the U correction in the potential was established following the method reported by Liechtenstein et al. [62]. The DOS results as a function of energy are presented in Fig. 8 for (a) La_2FeCoO_6 and (b) Tb_2FeCoO_6 compounds.

In Fig. 8 the zero-energy value is labeled as Fermi energy E_F. The correction applied to the exchange potential and correlation was U = 5.3 eV as it was the most in agreement with the experimental results [61]. The first feature observed in Fig. 8 for the total DOS in both materials is the asymmetric character of their electronic states between the up and down spin orientations. For spin up polarization the band gaps clearly correspond to an insulator with values $E_g^{La} > 3.6$ eV and $E_g^{Tb} > 3.8$ eV, while for spin down polarization the two materials exhibit semiconducting behavior with $E_g^{La^-} = 1.10$ eV and $E_g^{Tb^-} = 1.19$ eV. The obtained valence and conduction band configurations for the up and down spin orientations of the compounds with R = La and R = Tb are summarized in Fig. 9.

The generation of a spin-polarized charge transport channel has been theoretically predicted and experimentally measured in ferromagnetic semiconductors [88, 89]. This type of insulator-semiconductor distribution, which here we will call half-semiconductor in analogy with half-metallic behavior, is unusual in double

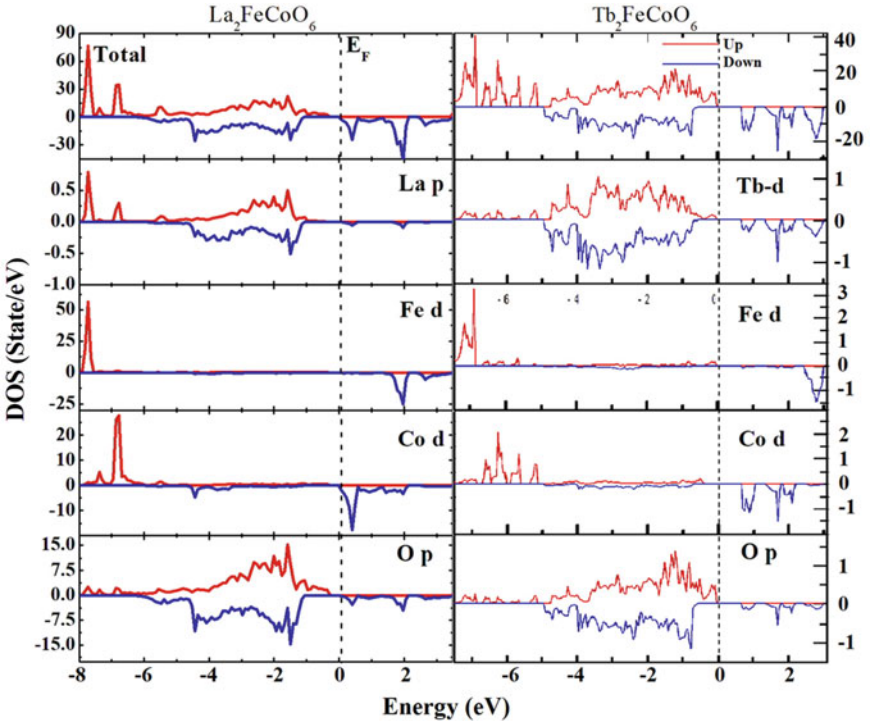

Fig. 8 Total and partial DOS calculated for **a** La_2FeCoO_6 and **b** Tb_2FeCoO_6 double perovskites

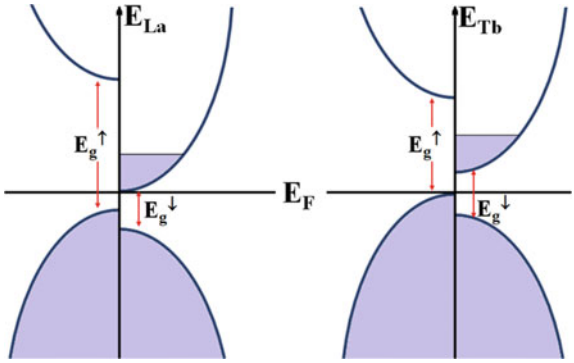

Fig. 9 Schematics of the valence and conduction bands with spin polarization for La_2FeCoO_6 and Tb_2FeCoO_6 ferrocobaltites

perovskites based on essentially metallic cations such as Fe and Co. Meanwhile, the occurrence of ferromagnetism and half-semiconductivity in the same crystalline structure is really interesting because it differs substantially from the case of dilute magnetic semiconductors, where there could be no guarantee of control in the positioning of magnetic moments in specific sites of the structural cells of the compound, besides the risk of having interstitial magnetic atoms outside the crystalline cells of the semiconductor material acting as matrix. These results allow inferring possible applications in devices that require magnetic control for the transport of both electric charge and spin moments, what we defined before as spintronics.

Analysis of the hybridizations between the outer electron shells of the atoms in the octahedrally coordinated structural octahedra with the oxygen anions suggest that the microscopic mechanism associated with the ferromagnetic behavior is of the super-exchange type between the high spin electrons of $Fe^{2+}{}_{3d}$ (e_g) and the low spin electrons of $Co^{4+}{}_{3d}$ (t_{2g}) mediated by the $O^{2-}{}_{2p}$ orbitals, as shown in the diagram in Fig. 10.

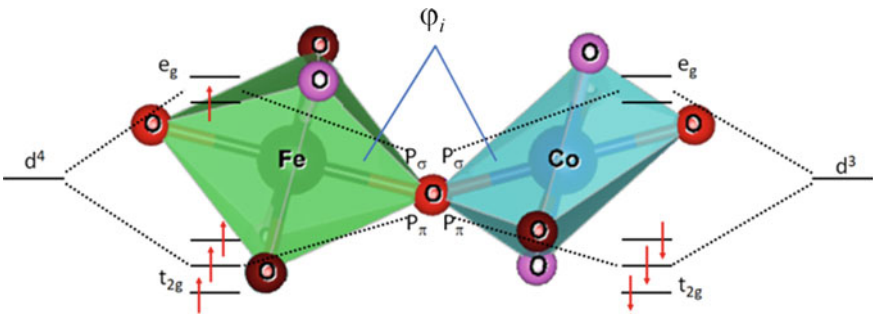

Fig. 10 Super-exchange interaction between e_g-moments of Fe and t_{2g}-moments of Co, giving rise to a weak ferromagnetic response in $(La,Tb)_2FeCoO_6$ complex perovskites

In this scenario, the interaction through the pi-bonds Fe-O-Co between the FeO_6 and CoO_6 octahedra, favours a total antiferromagnetic ordering, while through the sigma-bonds it can be observed that the bond angle 90° < Phi < 180° promotes ferromagnetic dominance through a Goodenough-Kanamori-Anderson type interaction [90].

4.5 Thermophysical Properties

An almost unexplored feature in double perovskite-type materials is the influence of the change in temperature and external pressure on their physical properties. These behaviors could provide relevant information in the study of the macroscopic responses that characterize this family of materials, so their modeling is of particular interest. Considering that during the electronic structure calculation process the equation of state was obtained, it was used in Debye's quasi-harmonic approximation formalism [91], facilitating the calculation of thermophysical properties for $(La,Tb)_2FeCoO_6$ materials in the 0 K < T < 900 K temperature regime, obtaining isobaric curves for applied pressures up to 5 GPa. The results of the specific heat at constant volume, $C_V(T,P)$, are shown in Fig. 11, where it can be observed that for T > 870 K the Dulong-Petit limit is reached, where the trend of the specific heat becomes independent of the temperature for values $C_{DP}{}^{La} = 491$ J/mol.K (Fig. 11a) and $C_{DP}{}^{Tb} = 493$ J/mol.K (Fig. 11b). It is evident from the insets of Figs. 11a,b that the specific heat at constant pressure, $C_p(T,P)$, has a behavior similar to that of $C_v(T,P)$ at T < 450 K but does not reach the Dulong-Petit limit in the temperature regime considered in the present work.

A literature search shows that more symmetric perovskite-type cells, such as cubic ones, present low C_{DP} values, with maximum values of 240 J/mol.K [30], which corresponds to 53% of the value obtained for monoclinic (pseudo-orthorhombic) structures of $(La,Tb)_2FeCoO_6$ materials. On the other hand, in perovskites with less

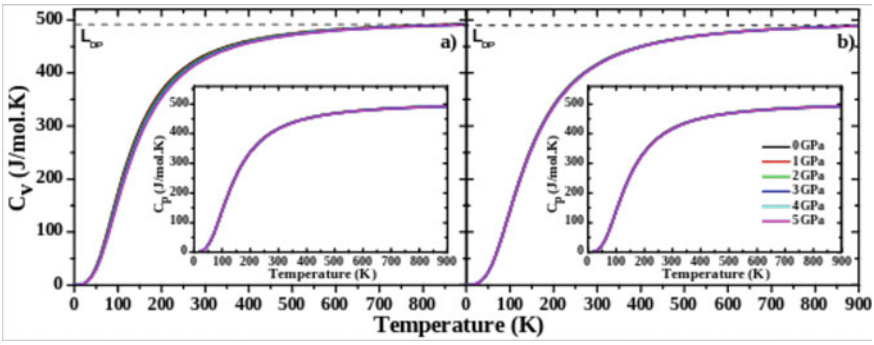

Fig. 11 Curves of $C_V(T,P)$ for the La_2FeCoO_6 (**a**) and Tb_2FeCoO_6 (**b**) double perovskites. The insets represent the respective $C_P(T,P)$ behaviors

symmetric structures the C_{DP} value exceeds 475 J/mol.K [53], showing that at low crystalline symmetries effects appear that give rise to nonharmonic contributions to the thermodynamic functions. This anharmonicity seems to increase with structural complexity [92, 93]. The density of states in Fig. 8 shows a very incipient contribution of the La-5p, La-5d and La-6 s orbitals to the specific heat, while the majority effect corresponds to the O-2p orbitals. This suggests that at high temperatures the electronic contributions could be superimposed on the phonon contributions produced by the vibrations in the cation-oxygen bonds, as a product of the large absorption of thermal energy, significantly increasing the value of the specific heat.

The dependence of the coefficient of thermal expansion with temperature and pressure calculated for $(La,Tb)_2FeCoO_6$ materials is shown in Fig. 12. The result shows that for values T < 300 K, the α(T,P) curves present an abrupt growth with increasing thermal energy, which is expected because, in addition to the strongly anisotropic character originating from the elastic properties of the material, the dramatic octahedral distortions, as well as the elongation of the structural cell along the crystallographic axes, contribute to the appearance of rotations and inclinations of the FeO_6 and CoO_6 octahedra. This behavior occurs because the increase in the thermal energy supplied generates a substantial increase in entropy, randomizing the physical properties and intensifying the phononic effects coming from the vibrations in the intermolecular bonds [67]. At T > 300 K the curve slows down and the change with increasing temperature is less significant because the growth in cell volume tends to stabilize at its maximum value, below which the increase in the coefficient of thermal expansion becomes asymptotic. On the other hand, the effect of the applied pressures partially neutralizes the vibrational activity, so that the increase in the value of the external pressure produces a systematic decrease in entropy which, in turn, shifts the thermal expansion curves towards lower values.

Figure 13 shows the behavior of the Grüneisen parameter γ(T,P), which grows nonlinearly with increasing thermal energy and decreases with increasing applied pressure. This result takes place due to the variations caused in the vibrational

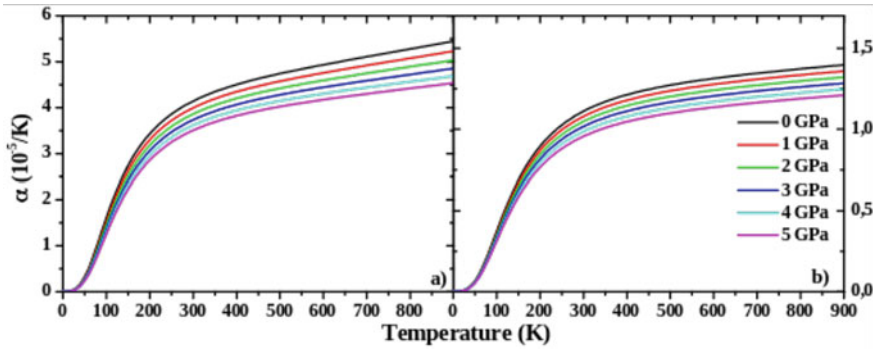

Fig. 12 Dependence of the coefficient of thermal expansion with temperature and pressure for the R_2FeCoO_6 ferrocobaltites with R = La (**a**) and R = Tb (**b**)

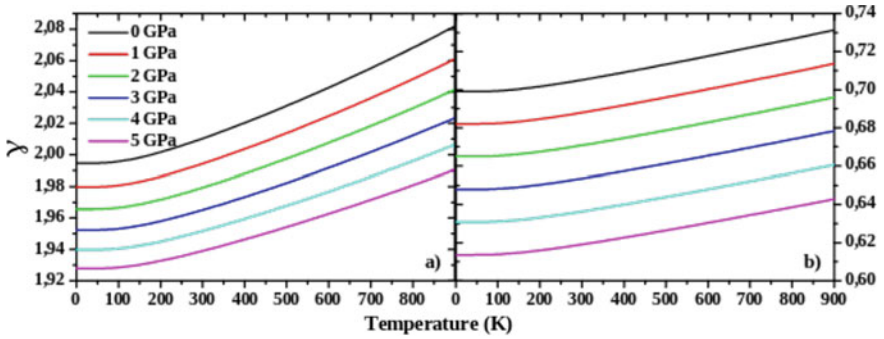

Fig. 13 Grüneisen parameter $\gamma(T,P)$ for the La_2FeCoO_6 (**a**) and Tb_2FeCoO_6 (**b**) materials

frequency of the crystal lattice, increasing the elastic waves of the system and increasing the Debye temperature and making the contribution of phonons large due to the low structural symmetry of the system [85]. On the other hand, as the pressure increases, the vibrational frequency of the cation-oxygen bonds throughout the structure also increases, while, simultaneously, the effect of the temperature increase expands the crystalline cells, causing an increase in the wavelength of these vibrations and promoting a decrease in the vibrational frequencies that shifts the Grüneisen parameter curves towards lower values.

5 Conclusions

Rietveld analysis of experimental XRD data of the solid-reacted $(La, Tb)_2FeCoO_6$ material reveals its crystallization in a monoclinic superstructure of the double perovskite type belonging to space group $P2_1/n$ (#14). The unit cell contains distortions due to differences in the sizes and orientation of the FeO_6 and CoO_6 octahedra, as well as the angles of the O-Fe-O and O-Co-O bonds along the basal and apical octahedral axes. Magnetic susceptibility reveals magnetic domain disorder effects, which cause ferromagnetic long-range order breaking, leading to irreversibility between curves measured through the ZFC and FC procedures, similar to those characterizing spin glasses. Meanwhile, the magnetization curves exhibit a hysteretic behavior characteristic of weak ferromagnetic materials, which is maintained up to room temperature, with values of the coercive field following Kneller's law in its dependence on temperature. On the other hand, the I-V curves obtained are semiconductor type with strong varistor type tendency, dramatically influenced by the granular nature of the materials.

The results of density of states calculations suggest that the material adopts an antiferromagnetic structure, in which the crystal field effects, and the type of chemical bonding promote a weak ferromagnetic response through a superexchange type mechanism such as that due to a Goodenough-Kanamori-Anderson type interaction.

The energy bands evidence an asymmetry between the spin up and down channels, creating a lower band-gap for one of the spin orientations than for the other, which gives rise to polarized spin currents in the semiconductor ferromagnetic material, suggesting its applicability in spintronic devices such as the so-called spin transistors.

References

1. Moore, G.E.: Cramming more components onto integrated circuits. Electronics **38**(8) April 19 (1965)
2. Kaur, I., Yadav, S., Singh, S., Kumar, V., Arora, S., Bhatnagar, D.: Solid State Phenom. **222**, 99 (2015)
3. Rahman, A.: A review on semiconductors including applications and temperature effects in semiconductors. Am. Sci. Res. J. Eng. Technol. Sci. (ASRJETS) **7**(1), 50–70 (2014)
4. Comstock, R.L.: Review modern magnetic materials in data storage. J. Mater. Sci: Mater. Electron. **13**, 509–523 (2002)
5. Wolf, S.A., Lu, J., Stan, M.R., Chen, E., Tregger, D.M.: The Promise of Nanomagnetics and Spintronics for Future Logic and Universal memory IEEE (2010)
6. Hirohata, A., Yamada, K., Nakatani, Y., Prejbeanu, I.-L., Diény, B., Pirro, P., Hillebrands, B.: Review on spintronics: Principles and device applications. J. Magn. Magn. Mater. **509**, 166711 (2020)
7. Baibich, M.N., Broto, J.M., Fert, A., Nguyen Van Dau, F., Petroff, F., Etienne, P., Creuzet, G., Friederich, A., Chazelas, J.: Phys. Rev. Lett. **61**, 2472 (1988)
8. Jin, S., Tiefel, T.H., McCormack, M., Fastnacht, R.A., Ramesh, R., Chen, L.H.: Thousandfold change in resistivity in magnetoresistive La-Ca-Mn-O films. Science **264**, 413–415 (1994)
9. Bonilla, C.M., Landínez Téllez, D.A., Arbey Rodríguez, J., Vera Lopez, E., Roa-Rojas, J.: Half-metallic behavior and electronic structure of Sr2CrMoO6 magnetic system, Physica B: Condensed Matter **398** (2), 208–211 (2007)
10. Nogués, J., Schuller, I.K.: Exchange bias. J. Magn. Magn. Mat. **192**, 203 (1999)
11. Palkar, V.R., Malik, S.K.: Solid State Commun. **134**, 783 (2005)
12. Wolf, S.A., Lu, J., Stan, M.R., Chen, E., Treger, D.M.: Proc IEEE **98**, 2155 (2010)
13. Bonanni, A., Dietl, T.: A story of high-temperature ferromagnetism in semiconductors. Chem. Soc. Rev. **39**, 528–539 (2010)
14. Chocho, J., Postava, K., Čada, M., Vanwolleghem, M., Halagačka, L., Lampin, J.-F., Pištora, J.: AIP Adv. **6**, 155021 (2016)
15. Chen, L., Yan, S., Xu, P.F., Lu, J., Wang, W.Z., Deng, J.J., Qian, X., Ji, Y., Zhao, J.H.: Appl. Phys. Lett. **95**, 182505 (2009)
16. Gupta, A., Zhang, R., Kumar, P., Kumar, V., Kumar, A.: Magnetochemistry **6**, 15 (2020)
17. Jiang, S., Hu, T., Gild, J., Zhou, N., Nie, J., Qin, M., Harrington, T., Vecchio, K., Luo, J.: Scr. Mater. **142**, 116 (2018)
18. Triana, C.A., Landínez Téllez, D.A., Roa-Rojas, J.: J. Alloys Compd. **516**, 179 (2012)
19. Cuervo Farfán, J.A., Parra Vargas, C.A., Viana, D.S.F., Milton, F.P., Garcia, D., Landínez Téllez, D.A., Roa-Rojas, J.: J. Mater. Sci: Mater. Electron. **29**, 20942 (2018)
20. Hazen, R.M.: Perovskites. Sci. Am. **258**, 74–81 (1988)
21. Llamosa, D.P., Landínez-Téllez, D.A., Roa-Rojas, J.: Magnetic and structural behavior of Sr2ZrMnO6 double perovskite. Phys B. **404**, 2726–2729 (2009)
22. Moya, X.A.V., Cardona, R., Hernández, J.I.V., Téllez, D.A.L., Roa-Rojas, J.: J. Electron. Mater. **47**(7), 3421–3429 (2018)
23. Cuervo Farfán, J.A., Aljure García, D.M., Cardona, R., Arbey Rodríguez, J., Landínez Téllez, D.A., Roa-Rojas, J.: J. Low Temper. Phys. **186** (5–6), 295–315 (2017)

24. Cuervo Farfán, J.A., Castellanos Acuña, H.E., Landínez Téllez, D.A., Roa-Rojas, J.: Structural, magnetic, and electrical features of the Nd2SrMn2TiO9 perovskite-like compound. Physica Status Solidi (b) **253** (6), 1127–1132 (2016)
25. Pilo, J., Miranda, A., Trejo, A., Carvajal, E., Cruz-Irisson, M.: Bidimensional perovskite systems for spintronic applications. J. Mol. Model. **23**, 322–325 (2017)
26. Maiti, A., Pal, A.J.: Effect of cation occupancy ordering in double perovskites to overcome hurdles in carrier transport: Cs2AgBiBr6 as a case study. J. Phys. Chem. C **125**(29), 16324–16333 (2021)
27. King, G., Woodward, P.M.: J. Mater. Chem. **20**, 5785–5796 (2010)
28. Benedek, N.A.: Inorg. Chem. **53**, 3769–3777 (2014)
29. Téllez, D.A.L., Buitrago, D.M., Barrera, E.W., Roa-Rojas, J.: Crystalline structure, magnetic response and electronic properties of RE2MgTiO6 (RE= Dy, Gd) double perovskites. J. Mol. Struct. **1067**, 205–209 (2014)
30. Deluque Toro, C.E., Mosquera Polo, A.S., Gil Rebaza, A.V., Landínez Téllez, D.A., Roa-Rojas, J.: J. Low Temp. Phys. **192**, 265–285 (2018)
31. Koehler, W.C., Wollan, E.O.: Neutron-diffraction study of the magnetic properties of perovskite-like compounds LaBO3. J. Phys. Chem. Solids **2**, 100 (1957)
32. Phokha, S., Pinitsoontorn, S., Maensiri, S., Rujirawat, S.: Structure, optical and magnetic properties of LaFeO3 nanoparticles prepared by polymerized complex method. J. Sol-Gel Sci. Technol. **71**, 333 (2014)
33. Acharya, S., Mondal, J., Ghosh, S., Roy, S.K., Chakrabarti, P.K.: Multiferroic Behavior of Lanthanum Orthoferrite (LaFeO3). Mater. Lett. **64**, 415 (2010)
34. Spaldin, N.A.: Multiferroics beyond electric-field control of magnetism. Proc. R. Soc. A **476**, 20190542 (2020). https://doi.org/10.1098/rspa.2019.0542
35. Dann, S.E., Currie, D.B., Weller, M.T., Thomas, M.F., Al-Rawwas, A.D.: J. Solid State Chem. **109**, 134–144 (1994)
36. Jonker, G.H., Van Santen, J.H.: Magnetic compounds with perovskite structure III. ferromagnetic compounds of cobalt. Physica **19**, 120 (1953)
37. Goodenough, J.B.: An interpretation of the magnetic properties of the perovskite-type mixed crystals La1−xSrxCoO3−λ. J. Chem. Phys. Solids **6**, 287 (1958)
38. Naiman, C.S., Gilmore, R., DiBartolo, B., Linz, A., Santoro, R.: Lanthanum rhodium and lanthanum cobalt oxides. J. Appl. Phys. **36**, 1044 (1965)
39. Korotin, M.A., Ezhov, S.Y., Solovyev, I.V., Anisimov, V.I., Khomskii, D.I., Sawatzky, G.A.: Electronic and spin configurations of Co3+ and Ni3+ ions in oxides of K2NiF4 structure: a magnetic susceptibility study, Phys. Rev. B54, 5309 (1996)
40. Durand, A.M., Belanger, D.P., Booth, C.H., Ye, F., Chi, S., Fernandez-Baca, J.A., Bhat, M.: J. Phys.: Condens. Matter **25**, 382203 (2013)
41. Sudheendra, L., Seikh, MD.M., Raju, A.R., Narayana, C., Rao, C.N.R.: Ferroelectrics **306**, 227 (2004)
42. Jaramillo Palacio, J.A., Muñoz Pulido, K.A., Arbey Rodríguez, J., Landínez Téllez, D.A., Roa-Rojas, J.: J. Adv. Dielectr. **11**, 2140003 (2021)
43. Fuh, H.-R., Weng, K.-C., Liu, Y.-P., Wang, Y.-K.: J. Alloys. Compd. **622**, 657 (2015)
44. Warshi, M.K., Mishra, V., Sagdeo, A., Mishra, V., Kumar, R., Sagdeo, P.R.: Structural, optical and electronic properties of $RFeO_3$. Ceram. Int. **44**, 8344–8349 (2018)
45. Tang, J., Ke, Y., He, W., Zhang, X., Zhang, W., Li, N., Cheng, Z.: Ultrafast photoinduced multimode antiferromagnetic spin dynamics in exchange-coupled Fe/RFeO3 (R = Er or Dy) heterostructures. Adv. Mater. **30**, 1706439 (2018)
46. Fita, I., Wisniewski, A., Puzniak, R., Zubov, E.E., Markovich, V., Gorodetsky, G.: Common exchange-biased spin switching mechanism in orthoferrites. Phys. Rev. B **98**, 094421 (2018)
47. Ke, Y.-J., Zhang, X.-Q., Ma, Y., Cheng, Z.-H.: Anisotropic magnetic entropy change in RFeO3 single crystals(R = Tb, Tm, or Y). Sci. Rep. **6**, 19775 (2016)
48. Panfilov, A.S., Grechnev, G.E., Lyogenkaya, A.A., Pashchenko, V.A., Zhuravleva, I.P., Vasylechko, L.O., Novoselov, D.: Magnetic properties of RCoO3 cobaltites (R = La, Pr, Nd, Sm, Eu). Effects of hydrostatic and chemical pressure. Physica B **553**, 80–87 (2019)

49. Knížek, K., Jirák, Z., Novák, P., de la Cruz, C.: Non-collinear magnetic structures of TbCoO3 and DyCoO3. Solid State Sci. **28**, 26–30 (2014)
50. Estrada Contreras, V.R., Alarcón Suesca, C.E., Deluque Toro, C.E., Landínez Téllez, D.A., Roa-Rojas, J.: Crystalline, ferromagnetic-semiconductor and electronic features of the terbium-based cobalt-ferrite Tb2FeCoO6. Ceram. Int. **47**, 14408–14417 (2021)
51. Cuervo Farfán, J., Arbey Rodriguez, J., Fajardo, F., Vera Lopez, E., Landínez Téllez, D.A., Roa-Rojas, J.: Physica B: Condensed Matter **404** (18), 2720–2722 (2009)
52. Gil Rebaza, A.V., Deluque Toro, C.E., Medina Chanduví, H.H., Landínez Téllezc, D.A., Roa-Rojas, J.: Thermodynamic evidence of the ferroelectric Berry phase in europium-based ferrobismuthite Eu2Bi2Fe4O12. J. Alloy Compd. **884**, 161114 (2021)
53. Cuervo Farfán, J.A., Deluque Toro, C.E., Parra Vargas, C.A., Landínez Téllez, D.A., Roa-Rojas, J.: Experimental and theoretical determination of physical properties in the Sm2Bi2Fe4O12 ferromagnetic semiconductor. J. Mater. Chem. C **8**, 14925–14939 (2020)
54. Nieto Camacho, J.A., Cardona Vásquez, J.A., Sarmiento Santos, A., Landínez Téllez, D.A., Roa-Rojas, J.: Study of the microstructure and the optical, electrical, and magnetic feature of the Dy2Bi2Fe4O12 ferromagnetic semiconductor. J. Mater. Res. Technol. **9**, 10686–10697 (2020)
55. Perdew, J.P., Zunger, A.: Phys. Rev. B **23**, 5048 (1981)
56. Vladimir, I.: Strong Coulomb Correlations in Electronic Structure Calculations: beyond the Local Density Approximation. Gordon and Breach, Amsterdam, The Netherlands (2000)
57. Blöchl, P.E.: Phys. Rev. B **50**, 17953 (1994)
58. Kresse, G., Joubert, J.: Phys. Rev. B **59**, 1758 (1999)
59. Heyd, J., Scuseria, G.E., Ernzerhof, M.: J. Chem. Phys. **118**, 8207 (2003)
60. Kresse, G., Furthmüller, J.: Comput. Mater. Sci. **6**, 15 (1996)
61. Deluque Toro, C.E., Muñoz Pulido, K.A., Arbey Rodríguez, J., Landínez Téllez, D.A., Roa-Rojas, J.: J. Low Temp. Phys. (2022). https://doi.org/10.1007/s10909-021-02649-w
62. Liechtenstein, A.I., Anisimov, V.I., Zaanen, J.: Phys. Rev. B **52**, R5467 (1995)
63. Monkhorst, H.J., Pack, J.D.: Phys. Rev. B **13**, 5188 (1976)
64. Methfessel, M., Paxton, A.T.: Phys. Rev. B **40**, 3616 (1986)
65. Murnaghan, F.D.: Proc. Natl. Acad. Sci. USA **30**, 244 (1944)
66. Deluque Toro, C.E., Mosquera Polo, A.S., Gil Rebaza, A.V., Landínez Téllez, D.A., Roa-Rojas, J.: Ab Initio study of the electronic structure, elastic properties, magnetic feature and thermodynamic properties of the Ba2NiMoO6 material. J. Low Temp. Phys. **192**, 265–285 (2018)
67. Deluque-Toro, C.E., Landínez-Téllez, D.A., Roa-Rojas, J.: Ab-initio analysis of magnetic, structural, electronic and thermodynamic properties of the Ba2TiMnO6 manganite. DYNA **85**, 27–36 (2018)
68. Glazer, A.M.: The classification of tilted octahedra in perovskites. Acta Cryst. **B28**, 3384 (1972)
69. Goldschmidt, V.M.: Die Gesetze der Krystallochemie. Naturwissenschaften **14**, 477 (1926)
70. Cerón, J.A.G., Rodríguez, J.A., Rosales-Rivera, A., Farfán, J.A.C., Vasquez, J.A.C.: J. Mater. Res. Technol. **8** (5), 3978–3987 (2019)
71. Landínez Téllez, D.A., Martínez Buitrago, D., Barrera, E.W., Roa-Rojas, J.: J. Mol. Struct. **1067**, 205–209 (2014)
72. Woodward, P.M.: Octahedral tilting in perovskites. I. Geometrical considerations, Acta Cryst. B **57**, 32–43 (1997)
73. Wang, X.L., James, M., Horvat, J., Dou, S.X.: Spin glass behaviour in ferromagnetic La2CoMnO6 perovskite manganite. Supercond. Sci. Technol. **15**, 427–430 (2002)
74. Corredor, L.T., Landínez-Téllez, D.A., Pimentel, J., Jr., Pureur, P., Roa-Rojas, J.: J. Mod. Phys. **2**, 154–157 (2011)
75. Ortiz-Diaz, O., Rodríguez Martínez, J.A., Fajardo, F., Landínez Téllez, D.A., Roa-Rojas, J.: Physica B: Condensed Matter **398**(2), 248–251 (2007)
76. Snoke, D.W.: Solid State Physics: Essential Concepts, Second Edition, pp. 526–597. Cambridge University Press (2020)

77. Bhowmik, R.N., Aneeshkumar, K.S.: Low temperature ferromagnetic properties, magnetic field induced spin order and random spin freezing effect in Ni1.5Fe1.5O4 ferrite; prepared at different pH values and annealing temperaturas. J. Magn. Magn. Mater. **460**, 177–187 (2018)
78. Khan, U., Adeela, N., Javed, K., Riaz, S., Ali, H., Iqbal, M., Han, X.F., Naseem, S.: Influence of cobalt doping on structural and magnetic properties of BiFeO3 nanoparticles. J. Nanopart. Res. **17**, 429 (2015)
79. Nunes, W.C., Folly, W.S.D., Sinnecker, J.P., Novak, M.A.: Temperature dependence of the coercive field in single-domain particle systems. Phys. Rev. B **70**, 014419 (2004)
80. Hauschild, J., Fritzsche, H., Bonn, S., Liu, Y.: Determination of the temperature dependence of the coercivity in Fe/Cr (110) multilayers. Appl. Phys. A **74**, S1541–S1543 (2002)
81. Felix, J.F., da Silva, E.F. Jr, De Vasconcelos, E.A., de Azevedo, W.M.: Tailoring the electrical properties of ZnO/Polyaniline heterostructures for device applications. J. Korean Phys. Soc. **58**, 1256–1260 (2011)
82. Vojta, A., Wen, Q., Clarke, D.R.: Influence of microstructural disorder on the current transport behavior of varistor ceramics. Comp. Mater. Sci. **6**, 51 (1996)
83. Pandey, R.K., Stapleton, W.A., Sutanto, I.: The effect of doping with some rare earth oxides on electrical features of ZnO. IEEE J. Electron Devi. Soc. **3**, 276–283 (2015)
84. Jüngel, A.: Quasi-hydrodynamic semiconductor equations (Springer Basel AG) (2001)
85. Alarcón-Suesca, C.E., Deluque Toro, C.E., Gil Rebaza, A.V., Landínez Téllez, D.A., Roa-Rojas, J.: J. Alloys Comp. **771**, 1080–1089 (2019)
86. Bonilla, M., Landínez Téllez, D.A., Arbey Rodríguez, J., Albino Aguiar, J., Roa-Rojas, J.: J. Magn. Magn. Mater. **320** (14), e397-e399 (2008)
87. Guss, P., Foster, M.E., Wong, B.M., Doty, F.P., Shah, K., Squillante, M.R., Shirwadkar, U., Hawrami, R., Tower, J., Yuan, D.: Results for aliovalent doping of CeBr 3 with Ca2+. J. Appl. Phys. **115**, 034908 (2014)
88. Bos, J.-W.: IUCrJ **4**, 712–713 (2017)
89. Toyosaki, H., Fukumura, T., Yamada, Y., Nakajima, K., Chikyow, T., Hasegawa, T., Koinuma, H., Kawasaki, M.: Nature Mater. **3**, 221–224 (2004)
90. Naruse, Y., Takamori, A.: Orbital phase perspective of Goodenough-Kanamori-Anderson Rules (GKA Rules) in superexchange interaction. ChemRxiv. Cambridge Open Engage, Cambridge (2020)
91. Deluque Toro, C.E., Landínez Téllez, D.A., Roa-Rojas, J.: DYNA, 85, 27 (2018)
92. Andritsos, E.I., Zarkadoula, E., Phillips, A.E., Dove, M.T., Walker, C.J., Brazhkin, V.V., Trachenko, K.: J. Phys.: Condens. Matter **25**, 235401 (2013)
93. Bryan, M.S., Pang, J.W.L., Larson, B.C., Chernatynskiy, A., Abernathy, D.L., Gofryk, K., Manley, M.E.: Phys. Rev. Mater. **3**, 065405 (2019)